HERSCHEL EXTREME LENSING LINE OBSERVATIONS: DYNAMICS OF TWO STRONGLY LENSED STAR-FORMING GALAXIES NEAR REDSHIFT $z = 2$[*]

James E. Rhoads[1], Sangeeta Malhotra[1], Sahar Allam[2], Chris Carilli[3], Françoise Combes[4], Keely Finkelstein[5], Steven Finkelstein[5], Brenda Frye[6], Maryvonne Gerin[7], Pierre Guillard[8], Nicole Nesvadba[8], Jane Rigby[9], Marco Spaans[10], and Michael A. Strauss[11]

[1] School of Earth and Space Exploration, Arizona State University, Tempe, AZ 85287, USA; James.Rhoads@asu.edu
[2] Space Telescope Institute, 3700 San Martin Drive, Baltimore, MD 21218, USA
[3] National Radio Astronomy Observatory, Socorro, NM 87801, USA
[4] Observatoire de Paris, LERMA, CNRS, 61 Av. de l'Observatoire, F-75014 Paris, France
[5] Department of Astronomy, University of Texas at Austin, 2515 Speedway, Stop C1400, Austin, TX 78712, USA
[6] Steward Observatory, University of Arizona, Tucson, AZ 85721, USA
[7] LERMA, 24 rue Lhomond, F-75231 Paris Cedex 05, France
[8] Institut d'Astrophysique Spatiale, Centre Universitaire d'Orsay, F-91405 Orsay Cedex, France
[9] NASA Goddard Space Flight Center, Greenbelt, MD 20771, USA
[10] Kapteyn Astronomical Institute, University of Groningen, 9700-AV Groningen, The Netherlands
[11] Department of Astrophysical Sciences, Princeton University, Peyton Hall, Princeton, NJ 08544, USA

ABSTRACT

We report on two regularly rotating galaxies at redshift $z \approx 2$, using high-resolution spectra of the bright [C II] $158\,\mu m$ emission line from the HIFI instrument on the *Herschel Space Observatory*. Both SDSS090122.37+181432.3 ("S0901") and SDSSJ120602.09+514229.5 ("the Clone") are strongly lensed and show the double-horned line profile that is typical of rotating gas disks. Using a parametric disk model to fit the emission line profiles, we find that S0901 has a rotation speed of $v \sin(i) \approx 120 \pm 7\,\mathrm{km\,s^{-1}}$ and a gas velocity dispersion of $\sigma_g < 23\,\mathrm{km\,s^{-1}}$ (1σ). The best-fitting model for the Clone is a rotationally supported disk having $v \sin(i) \approx 79 \pm 11\,\mathrm{km\,s^{-1}}$ and $\sigma_g \lesssim 4\,\mathrm{km\,s^{-1}}$ (1σ). However, the Clone is also consistent with a family of dispersion-dominated models having $\sigma_g = 92 \pm 20\,\mathrm{km\,s^{-1}}$. Our results showcase the potential of the [C II] line as a kinematic probe of high-redshift galaxy dynamics: [C II] is bright, accessible to heterodyne receivers with exquisite velocity resolution, and traces dense star-forming interstellar gas. Future [C II] line observations with ALMA would offer the further advantage of spatial resolution, allowing a clearer separation between rotation and velocity dispersion.

Key words: galaxies: evolution – galaxies: formation – galaxies: high-redshift

Online-only material: color figures

1. INTRODUCTION

Typical star-forming galaxies in the nearby universe are supported by systematic rotation with random velocities playing a relatively minor role. This indicates a degree of maturity—the galaxies are old and established, and their reservoirs of star-forming gas are dominated by material that was accreted at least one orbital time ago. However, at the epoch when cosmic star formation reached its peak, it is likely that galaxies were still accreting gas rapidly. The relative roles of rotation and velocity dispersion in providing support to such galaxies could thus be significantly different. Certainly, the morphologies of star-forming galaxies at $z \sim 2$ suggest *some* differences in their typical properties: regular spirals constituted a much smaller fraction of galaxies at $z \sim 2$ than they do today.

Dynamical observations of star-forming galaxies at $z \sim 2$ are challenging. One successful approach has been to study strong rest-frame optical emission lines, which are redshifted to near-IR wavelengths (e.g., Förster Schreiber et al. 2009; Lehnert et al. 2013; Rhoads et al. 2014). Spatial resolution is generally limited by seeing to $\gtrsim 0\farcs5$, which yields a few resolution elements across the disk of the galaxy. For a minority of cases it has been possible to achieve significantly higher spatial resolution, either by using adaptive optics (e.g., Law et al. 2009), or by observing strongly lensed galaxies (Jones et al. 2010; Frye et al. 2012; Wuyts et al. 2012; Jones et al. 2013). Spectral resolution is also usually modest ($R \lesssim 6000$, corresponding to $\Delta v \gtrsim 50\,\mathrm{km\,s^{-1}}$) since the faint flux levels of $z \sim 2$ emission lines usually preclude the lower sensitivity of high-resolution spectrographs.

Here we adopt a complementary approach to studying the dynamical support of $z \sim 2$ star-forming galaxies. We use [C II] $158\,\mu m$ line observations from the *Herschel* Extreme Lensing Line Observations (HELLO) program (Malhotra et al. 2014), obtained using the HIFI instrument (de Graauw et al. 2010) on the *Herschel Space Observatory* (Pilbratt et al. 2010). The resulting line profiles are at exquisite spectral resolution, though entirely unresolved spatially. In the present paper we analyze the galaxies SDSS090122.37+181432.3 (Diehl et al. 2009, hereafter S0901) and SDSSJ120602.09+514229.5, also called "the Clone" (Lin et al. 2009). Both galaxies show the double-horned rotation profile that is characteristic of rotationally supported disks. The shape of this profile contains considerable information on the disks' dynamical properties.

C^+ is the main coolant of neutral gas in galaxies. Typically, 0.3% of far-infrared luminosity emerges in the [C II] $158\,\mu m$ line. Thus, it can be an excellent tracer of interstellar medium (ISM) kinematics. The question then is where the [C II] emission comes from. [C II] can trace neutral gas, since carbon has a lower ionization potential than hydrogen. The brightest [C II]

---

emission in a galaxy comes from photon-dominated regions (PDRs). These are surface layers of dense molecular clouds, where UV light from nearby star formation is dissociating molecular gas. [C ɪɪ] probes primarily a density range from a few cm^{-3}, which is required to excite the transition, up to the critical density of $\sim 10^{3.5} \, cm^{-3}$. The integrated [C ɪɪ] emission from whole galaxies includes potentially important contributions from diffuse ionized gas (Bennett et al. 1994) and also from diffuse H ɪ, although the fractions are debated (e.g., Madden et al. 1993; Heiles 1994; Contursi et al. 2002). The radial distribution of [C ɪɪ] in nearby galaxies generally follows CO (e.g., Kramer et al. 2013; Pineda et al. 2013, for M33 and the Milky Way, respectively), although [C ɪɪ] emission has also been observed in outflows (Contursi et al. 2013) and in turbulently heated gas in nearby radio galaxies (P. Guillard et al. 2014, in preparation). The galaxies studied in this paper have typical [C ɪɪ]/FIR ratios (Malhotra et al. 2014), and do not show the [C ɪɪ] deficiency seen in some luminous nearby systems (e.g., Malhotra et al. 1997, 2001; Carilli & Walter 2013).

We describe our sample and observations in Section 2. We discuss our Markov chain Monte Carlo (MCMC) spectral line fitting methods and results in Section 3, and compare them to Hα observations of the same objects in Section 4. We close with a discussion of implications and future directions in Section 5. Throughout the paper, we adopt a Λ-CDM "concordance cosmology" with $\Omega_M = 0.27$, $\Omega_\Lambda = 0.73$, and $H_0 = 71 \, km \, s^{-1} \, Mpc^{-1}$.

2. THE SAMPLE AND THE OBSERVATIONS

2.1. Sample Selection and Properties

The full HELLO sample consists of 15 strongly lensed galaxies, at redshifts $1.0 < z < 3.0$. The sample was selected to span a range of both star formation rate (SFR) and redshift. All HELLO targets were observed using the HIFI Wide Band Spectrometer (WBS) backend. We describe the HIFI observations of the full sample in Malhotra et al. (2014). Here, we focus our attention on the two objects (S0901 and the Clone) that show distinct double peaks in their line profiles. We summarize the key observational information for these two objects below. Both were identified as candidate lens systems through a search for blue objects near luminous red galaxies (LRGs) in Sloan Digital Sky Survey (SDSS) imaging, followed by visual inspection for arc-like morphology (Diehl et al. 2009; Lin et al. 2009).

S0901 was confirmed as a strongly lensed galaxy at redshift $z = 2.2558$ by Diehl et al. (2009). The lens is a galaxy group, dominated by a LRG at $z = 0.3459$ (Diehl et al. 2009), and containing another half dozen smaller galaxies. The lensed galaxy appears as a $17''$ long arc, oriented primarily north–south, and located east of the lensing galaxy. Diehl et al. (2009) identify two main components of the arc (labeled "b" and "d" in their published image), and measure its Einstein radius as $7''.7 \pm 1''.1$. *Hubble Space Telescope* (*HST*) imaging (from program 11602, PI: S. Allam) shows considerable substructure (as is usual for star-forming galaxies observed in the rest-frame UV), as well as a possible counterimage $4''$ west of the LRG, and a foreground galaxy superposed on arc component "b." Hainline et al. (2009) published the lensed galaxy's rest-frame optical spectrum, which shows prominent emission lines of Hα and [N ɪɪ], as well as weaker lines of [O ɪɪɪ], Hβ, [O ɪɪ], and [Ne ɪɪɪ]. Hainline et al. (2009) note that [N ɪɪ]/Hα $\gtrsim 0.65$, implying the presence of an active galactic nucleus (AGN). On the other hand, the object's mid-infrared spectrum shows strong polycyclic

aromatic hydrocarbon (PAH) emission features, suggesting that the dust heating is dominated by star formation rather than by the AGN (Fadely et al. 2010). The gravitational lensing amplification of S0901 does not appear to be formally published. Available estimates range from amplification $\mu \sim 8$ (Fadely et al. (2010), quoting from work in progress by A. West et al.), to $\mu \sim 6$ (E. Buckley-Geer 2013, private communication), while inspection of the *HST* imaging suggests that larger amplifications are plausible. Where needed, we use a fiducial value $\mu = 6$, but we retain μ in our equations to show explicitly how the results will scale for other μ. Apart from the inferred SFR of S0901, our primary conclusions in the present paper are essentially independent of the lensing amplification.

The Clone (SDSSJ120602.09+514229.5) was first identified as a strongly lensed galaxy at redshift $z = 2.00$ by Lin et al. (2009). The lens is again a group, here with three identified members, dominated by an LRG at $z = 0.422$ (Lin et al. 2009). The arc has three primary components which together span about 120°, plus a small counterimage. Lin et al. (2009) labeled the components of the main arc as A1, A2, A3, and the counterimage as A4. They modeled the lensing geometry based on ground-based imaging, finding an Einstein radius $3''.82$, and an amplification factor $\mu = 27 \pm 1$. The lensed galaxy's rest-frame optical spectrum (Hainline et al. 2009) is that of a star-forming galaxy, with no evidence for AGN activity. Detected lines include Hα, Hβ, [O ɪɪ], [O ɪɪɪ], and [S ɪɪ]. The Clone's mid-IR spectrum is again that of a normal star-forming galaxy, with prominent PAH emission features (Fadely et al. 2010). More recent lens modeling, using higher-resolution *HST* images (Jones et al. 2010), gives a refined amplification $\mu = 28.1 \pm 1.4$. (This is the total amplification for all lensed images combined, as appropriate for our spatially unresolved HIFI observation.)

Hainline et al. (2009) also estimated the SFR for the Clone. They scaled from the Hα flux, assumed a Chabrier (2003) initial mass function, and corrected for gravitational lensing amplification (μ, see below). They obtained SFR = 32 $M_\odot \, yr^{-1}$ before dust correction and SFR = 64–75 $M_\odot \, yr^{-1}$ after dust correction (depending on the adopted reddening indicator). They did not estimate a SFR for S0901, given their concerns about the possible role of an AGN. We can obtain a crude upper limit on the SFR of S0901 by neglecting AGN contributions to Hα and applying the same scalings used for the Clone. This yields $\sim 135 \, M_\odot \, yr^{-1} \times (6/\mu)$, prior to any dust correction.

2.2. Herschel Observations

We observed the *HELLO* sample using the HIFI WBS with 1.10 MHz resolution. We used dual beam switching with fast chopping to achieve the best possible baselines in our spectra. For S0901, we used mixer band 1b and a total observing time of 3000 s, of which 885 s was on-source integration time. For the Clone, we used mixer band 1b with a total observing time of 6200 s, of which 1977 s was on-source integration time. Our data reduction—which we discuss in greater detail in Malhotra et al. (2014)—followed mostly standard HIFI procedures. The last step of this analysis was to fit and subtract a baseline from each spectrum. This means that the spectra used in the present paper are "line-only" spectra, insensitive to the presence of continuum emission.

The HIFI WBS offers an intrinsic velocity resolution of $<0.6 \, km \, s^{-1}$ at the frequency of the redshifted [C ɪɪ] line in our targets. However, each 1.10 MHz resolution element has a signal-to-noise ratio (S/N) < 1 in our data. Our ability to distinguish fine detail in the spectral line profiles is therefore
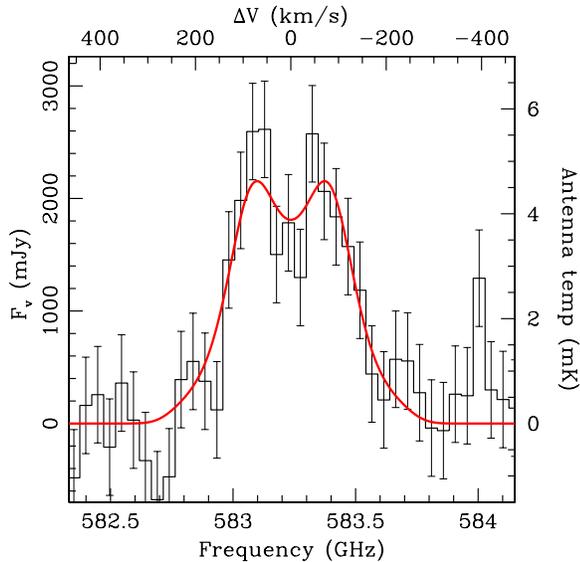
Figure 1. HIFI spectrum of the [C II] 158 μm line from SDSS090122.37+181432.3, binned to 25 km s⁻¹ resolution (black histogram). Plotted error bars are derived empirically from the rms of the spectrum, measured at line-free frequencies. The overplotted model is a centrally concentrated disk model, with $v_{d,1/2} = 121$ km s⁻¹, $\sigma_g = 29$ km s⁻¹, and a negligible halo component. The resulting ratio of circular speed to velocity dispersion is 4.2, and at the 95% confidence level, the ratio is >2.7.
(A color version of this figure is available in the online journal.)

effectively limited by sensitivity, since we can detect features only when we combine enough frequency channels to get S/N of a few in the feature.

We plot the [C II] spectrum of S0901 in Figure 1 and of the Clone in Figure 2, both at 25 km s⁻¹ binning. S0901 has a flux of 1.3 K km s⁻¹ (1.2×10^{-17} W m⁻²), and yields a S/N $\gtrsim 4$ per bin for 11 bins above half-maximum intensity. The Clone is fainter, with a flux of 0.3 K km s⁻¹ (3.2×10^{-17} W m⁻²), and yields S/N ~ 3 per bin for 6 bins above half-maximum intensity. We discuss these flux measurements further in Malhotra et al. (2014), in the context of the full HELLO sample. In addition to the spectra, we plot model line profiles from our fitting procedures in Figures 1 and 2.

3. EMISSION LINE PROFILE FITTING

The observed [C II] emission line profiles depend on the rotation curves of the lensed galaxies. They also depend on the spatial distribution of the emitting gas, which determines how the different parts of the rotation curve are weighted in forming the line profile. To model the line profiles, we adopt commonly used fitting functions for the distributions of both emitting material and of mass (which in turn determines the rotation curve).

For the radial distribution of [C II] surface brightness, we have assumed an exponential disk model ($\Sigma_{[C II]} = \Sigma_0 \exp(-r/r_{[C II]})$), which is able to produce models that fit the observed lines well (see below). Of course, this does not mean that the gas distribution *must* follow an exponential distribution. Different tracers of galaxies' interstellar gas often follow different distributions. Neutral hydrogen (H I) tends to have a spatially extended distribution. Molecular gas can be centrally concentrated (as in many starbursts and ultraluminous infrared galaxies), or can show ring features, as in both our own Galaxy and M31. Hα comes primarily from dense, ionized gas, and often shows com-
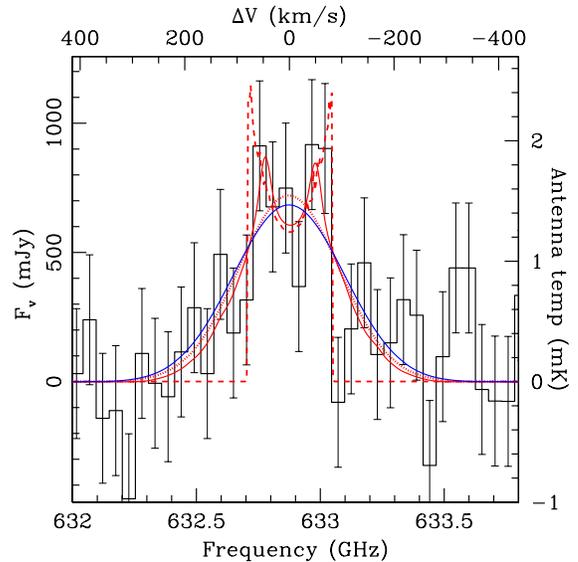

Figure 2. Like Figure 1, but for SDSSJ120602.09+514229.5 (the Clone). Here, the signal-to-noise ratio is lower, and a range of models provide acceptable fits to the data. The modeling procedures are described in Section 3. We plot four representative cases. The dashed red line shows the model with the highest likelihood among our MCMC simulation results, a "pure" double-horned line profile where most of the emitting gas is on the flat part of the rotation curve, and the velocity dispersion is very small. If we consider only models with $\sigma_g > 7$ km s⁻¹ (motivated by typical motions within thin disks), the best fit (shown as the solid red line) remains double-horned, but with very extended wings, here driven by a rotation curve that continues rising beyond the spatial extent of the emitting gas. Finally, we plot two dispersion-dominated models. The first (red dotted line) is effectively a pure Gaussian, with $\sigma_g = 98$ km s⁻¹ and negligible rotation. The second (blue solid line) matches the results of Jones et al. (2013), from spatially resolved near-IR spectra, having $v_{d,1/2} = 70$ km s⁻¹, $x_{ds} = 1.1$, and $\sigma_g = 94$ km s⁻¹. The ratio of circular speed to velocity dispersion spans a wide range for these and other acceptable models of the Clone's [C II] emission (see Figure 3).
(A color version of this figure is available in the online journal.)

plex and patchy distributions that trace the distribution of young star-forming regions.

A double-horned line profile basically requires that most of the emitting material be in significant motion with respect to the center of mass. Given that galactic rotation curves rise steeply in the central regions and then flatten out, there are two "usual" ways to achieve this. First, the gas can be in an extended disk, with most of the mass on the flat part of the rotation curve. This is the common case for H I (Springob et al. 2005). Second, the gas can be in a more compact ring-like configuration, with little material to emit in the regions where rotation is slow. This has been observed, e.g., for CO line emission in NGC 759 (Wiklind et al. 1997). Since [C II] 158 μm emission comes in some combination from the diffuse warm neutral medium, PDRs at molecular cloud surfaces, *and* ionized regions, we do not expect a simple analogy with other main ISM tracers. We begin by considering the extended disk possibility in detail, and then examine how our conclusions would be affected for the case of a [C II] ring.

We model the rotation curve using a disk + halo model for the gravitating mass. The halo has a mass volume density of $\rho \propto (1 + r/r_h)^{-2}$ and an asymptotic rotation speed of v_h. The disk component has a mass surface density of $\Sigma \propto \exp(-r/r_d)$ and a peak rotation speed of v_d. We can relate v_d to other disk parameters as $v_d \approx 0.5463\sqrt{GM_{disk}/r_d}$, where M_{disk} is the total mass of the exponential disk. v_d corresponds to the

circular speed for the disk mass interior to $r = 1.7933 r_d$.[12] We model the line-of-sight gas velocity dispersion (due to thermal *and* turbulent motions) as a Gaussian with rms width σ_g, which is convolved with the line profile produced by ordered rotation.

Because our targets are spatially unresolved in HIFI data, our predicted line profile is insensitive to a global rescaling of all radii by a common, constant factor. We therefore fix the scale length $r_{[C\,II]}$ of the surface brightness distribution throughout the modeling, and rewrite the scale lengths of the disk and halo in dimensionless form as $x_d \equiv r_d/r_{[C\,II]}$ and $x_h \equiv r_h/r_{[C\,II]}$. Similarly, the line profile depends on the line-of-sight velocity $v\sin(i)$ (where i is the inclination angle of the disk) but cannot distinguish changes in i from changes in v.

The line shape is then determined by a total of five free parameters: Three velocities (v_d, v_h, and σ_g), and two scale length ratios (x_d and x_h). We need two further parameters, the redshift z and total line flux $f_{[C\,II]}$, to completely specify the line.

Before fitting the disk+halo rotation curve models, we recast the three velocity parameters in a new form that reduces correlated uncertainties in the parameter space. Since the observed line profile is determined by gas kinematics *where the light is emitted*, we define the rotational speed contributions due to the halo and disk, $v_{h,1/2}$ and $v_{d,1/2}$ measured at the half-light radius of the [C II] disk (which is $r_{[C\,II],1/2} = 1.66 r_{[C\,II]}$). We then define the *total ordered rotation speed* $v_{c,1/2}$ at the half-light radius by

$$v_{c,1/2}^2 = v_{h,1/2}^2 + v_{d,1/2}^2. \tag{1}$$

We further define

$$v_{1/2}^2 = v_{c,1/2}^2 + \sigma_g^2 = v_{h,1/2}^2 + v_{d,1/2}^2 + \sigma_g^2. \tag{2}$$

The parameter $v_{1/2}$ now contains essentially all the information required to determine the [C II] line width. The relative importance of random and ordered motions is captured by the velocity ratio

$$y_{\sigma c} = \sigma_g/v_{c,1/2} \tag{3}$$

while the relative importance of disk and halo terms in the potential is captured by

$$y_{dh} = v_{d,1/2}/v_{h,1/2}. \tag{4}$$

The transformation is essentially from Cartesian coordinates $(v_{h,1/2}, v_{d,1/2}, \sigma)$ to spherical polar coordinates $(v_{1/2}, y_{\sigma c}, y_{dh})$ for the three-space of velocity parameters, with the y parameters corresponding to (co)tangents of two angles.

The final set of parameters for fitting then becomes $\{v_{1/2}, y_{\sigma c}, y_{dh}, x_d, x_h, z, f_{[C\,II]}\}$. By recasting the three velocity parameters, we eliminate major degeneracies between v_d, v_h, and σ_g, all of which have the same lowest-order effect of increasing the model line width. Now, $v_{1/2}$ determines line width, while the remaining parameters control the shape of the line—whether it is singly or doubly peaked, the splitting of the peaks and depth of the gap between them, and the shape of the high-velocity line wings.

We fitted the rotation curve models to the data using a MCMC approach (more specifically, the Metropolis–Hastings algorithm). In brief, the method consists of a chain of random steps in our parameter space. In each step, the algorithm first identifies a trial solution that is offset from the current solution by some randomly determined amount. The likelihood of the

trial solution is compared to that of the current solution. The trial solution is adopted as the new solution whenever its likelihood is higher. If its likelihood is lower, it may still be adopted as the new solution, with a probability equal to the ratio of likelihoods. After many steps, the distribution of accepted points provides an unbiased estimator for the probability distribution of the model parameters. Since consecutive steps of the chain are highly correlated, we record the state of the chain every 100 steps, so that the autocorrelation among the recorded points in parameter space is weak.

Over 99% of the MCMC solutions for S0901 under the disk+halo rotation curve model lie in a single region of parameter space, where rotation dominates over a small or negligible amount of random motion. A representative fit is shown in Figure 1, and its parameters are given in Table 1. The distribution of MCMC samples in the ($v_{1/2}$, σ_g) plane is shown in Figure 3. Only 5% of the samples have $\sigma_g > 43.5\,\mathrm{km\,s^{-1}}$; 1% have $\sigma_g > 60\,\mathrm{km\,s^{-1}}$; and only 0.5% have $\sigma_g > v_{1/2}$. Moreover, the rotational motions are usually dominated by the disk component (with $\langle \log(y_{dh}) \rangle = 0.92$, and with $y_{dh} > 1$ in 85% of samples).

This conclusion is robust, being readily explained by examination of the observed line profile. The line is double-horned with a central dip, and with rotation curve sides that are steep but not vertical. Figure 4 shows examples of the line profiles produced by three simple kinematic models, each of which is dominated by a single component. Models dominated by velocity dispersion (σ_g) are expected to be single-peaked. Models dominated by a halo (with small core radius and without a significant disk contribution) would have vertical sides, except for the influence of the velocity dispersion. Under our adopted rotation curve model, the best way to get a double-peaked profile with slanting sides is to have a rotation curve that rises to a peak (driven by the disk component) and then declines toward somewhat smaller rotation speeds (perhaps dominated by the halo component).

Our [C II] line profile fitting in the Clone yields a range of viable models. The maximum likelihood fits are double-peaked models with very small velocity dispersions, much like the fits for S0901. However, these models occur in a rather small volume of the sampled parameter space. The MCMC fitting for the Clone also yields single-peaked, dispersion-dominated fits (with $y_{\sigma c} > 1$) in about 45% of all samples. These have appreciably lower likelihoods, but occupy a large volume in parameter space. For the Clone, we have plotted a few different models, all statistically acceptable fits to the data. These include the maximum likelihood model identified, which is dominated by a disk with $v_{d,1/2} = 78\,\mathrm{km\,s^{-1}}$ and $x_{ds} = 1.52$, and has $\sigma_g \approx 1\,\mathrm{km\,s^{-1}}$. We plot also a second double-peaked profile and two dispersion-dominated single peaked profiles. Parameters for all are summarized in Table 1. The last of these plotted models was selected to be consistent with the parameters that Jones et al. (2010) derived based on Hα observations (see Section 4).

Our fitting yields other parameters in addition to $v_{1/2}$ and σ_g. The most robust and model-independent are the redshifts (which we report in the local standard of rest [LSR] frame). For S0901, we find $z_{[C\,II]} = 2.25860 \pm 0.00007$. This matches precisely the rest-frame optical redshift ($z = 2.2586 \pm \sim 0.0001$; Hainline et al. 2009) derived from Hα, [N II], and [O III] emission lines, while it is slightly higher than the rest-UV redshift of $z = 2.2558 \pm 0.0003$ (Diehl et al. 2009). This gives a net blueshift of $\Delta v \approx 260 \pm 30\,\mathrm{km\,s^{-1}}$ for the UV spectral features, relative to [C II]. The Diehl et al. (2009) redshift is from a

---

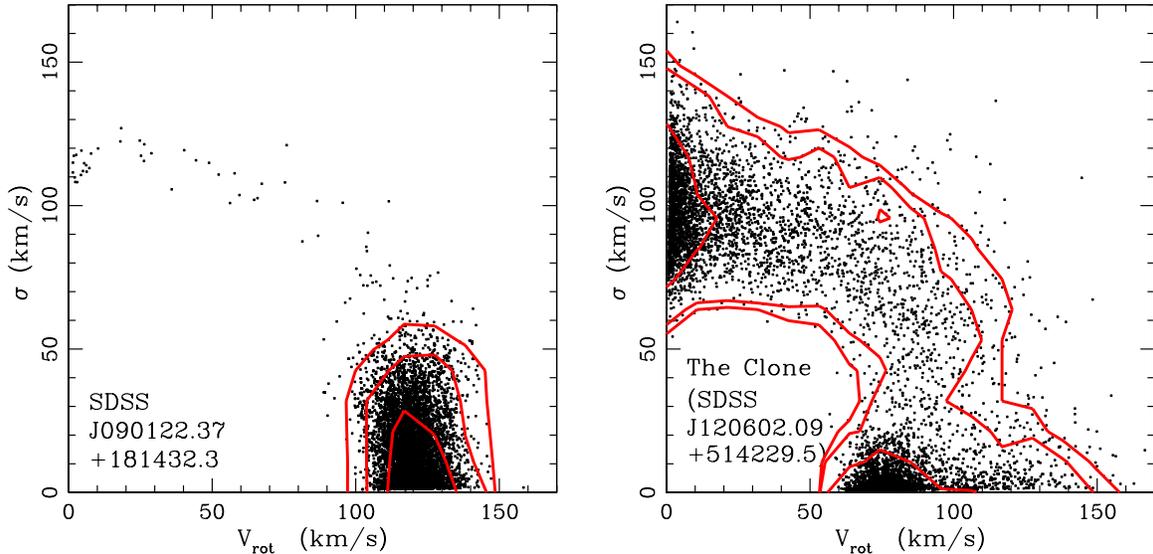[12] Rephrased, the rotation curve for a pure exponential disk peaks near 1.8 scale lengths.

Figure 3. Probability distribution for the kinematic support parameters v_{rot} and σ_g for SDSS090122.37+181432.3 (left) and for the Clone (SDSSJ120602.09+514229.5, right), based on our disk+halo rotation curve model (Section 3). The plotted points show nearly 8000 samples from our Markov chain Monte Carlo parameter fitting code. Plotted contours enclose 68%, 95%, and 98% confidence regions. For S0901, rotationally supported solutions are strongly favored, with only 0.5% of the samples having $\sigma_g > v_{rot}$. For the Clone, which has a lower signal-to-noise ratio, the corresponding fraction is $\sim$44%.
(A color version of this figure is available in the online journal.)

Table 1
Parameters of Selected Model Fits Plotted in the Figures

Object	$v_{d,1/2}$ (km s^{-1})	$v_{h,1/2}$ (km s^{-1})	σ_g (km s^{-1})	x_d	x_h	Flux (K km s^{-1})	$\Delta \log(L)$[a]	Line Style
SDSS 0901	**121**	2	**29**	**0.11**	9.3	1.359	0	Solid red
The Clone	**78**	2	**1**	1.52	0.7	0.2657	0	Dashed red
The Clone	**20**	**100**	**8**	**0.07**	**6.2**	0.365	−1.4	Solid red
The Clone	0	2	98	0.5	0.26	0.371	−3.3	Dotted red
The Clone	**70**	2	94	**1.1**	0.05	0.386	−3.44	Solid blue
(None)	**75**	1	7.5	**0.22**	0.1	$\cdots$	$\cdots$	Black
(None)	1	**75**	7.5	1	**0.1**	$\cdots$	$\cdots$	Blue
(None)	10	10	**75**	1	1	$\cdots$	$\cdots$	Red

Notes. We include the best-fitting model for S0901 (top line, plotted in Figure 1); four representative model fits for the Clone (lines 2–5, plotted in Figure 2); and three sample "toy models" chosen to illustrate features of the rotation curve model (lines 6–8, plotted in Figure 4). In each case, parameters associated with the dominant component(s) determining the line profile shape are given in bold, and small changes to the remaining parameters would have small or negligible effects on the model line profile.
[a] $\Delta \log(L)$ is the log of likelihood, relative to the maximum likelihood model identified for the same observed line.

cross-correlation of the S0901 spectrum with a template from Shapley et al. (2003), making it a weighted average of the Lyα line redshift and the redshift from UV absorption lines (which are, individually, mostly too faint to measure well in S0901). To the extent that this represents a Lyα redshift, it is an unusual result—Lyα is generally redshifted with respect to other velocity tracers (e.g., Shapley et al. 2003; McLinden et al. 2011), and a blueshift of this magnitude for Lyα would be worth further investigation.

For the Clone, we find $z = 2.0030 \pm 0.00009$. This can be compared to the measurements $z = 2.0001 \pm 0.0006$ and $z = 2.0010 \pm 0.0009$, both from rest-UV absorption lines reported by Lin et al. (2009) but based on different spectra taken at two different telescopes. Comparing our [C II] redshift to the weighted average, $z_{UV} = 2.0004 \pm 0.0005$, we infer that the gas responsible for the UV absorption lines is blueshifted by 260 ± 60 km s^{-1} with respect to the [C II] emitting gas. This is typical of the absorption line blueshifts that are seen in many

high-redshift galaxies, and that are thought to be caused by absorption by gas in a galactic wind (e.g., Pettini et al. 2001; Frye et al. 2002; Shapley et al. 2003).

Finally, we consider how our conclusions would be affected by changing some of the assumptions behind our rotating disk model. First, we explore the possible effects of differential gravitational magnification by applying separate amplification factors to the approaching and receding portions of the galaxy. Taking the overall mean amplification to be $\bar{\mu}$ and the ratio of red-side to blue-side amplification to be μ_a, we have amplifications of $2\bar{\mu}/(1+\mu_a)$ for the blue side and $2\mu_a\bar{\mu}/(1+\mu_a)$ for the red side. We apply this differential magnification to the predicted line profile before accounting for the velocity dispersion, thus avoiding a sharp step function at the systemic velocity.

For S0901, we find that the distribution of this new parameter is sharply peaked near unity: 98.64% of simulated samples are in a primary peak centered at $\mu_a = 0.92$, with dispersion of
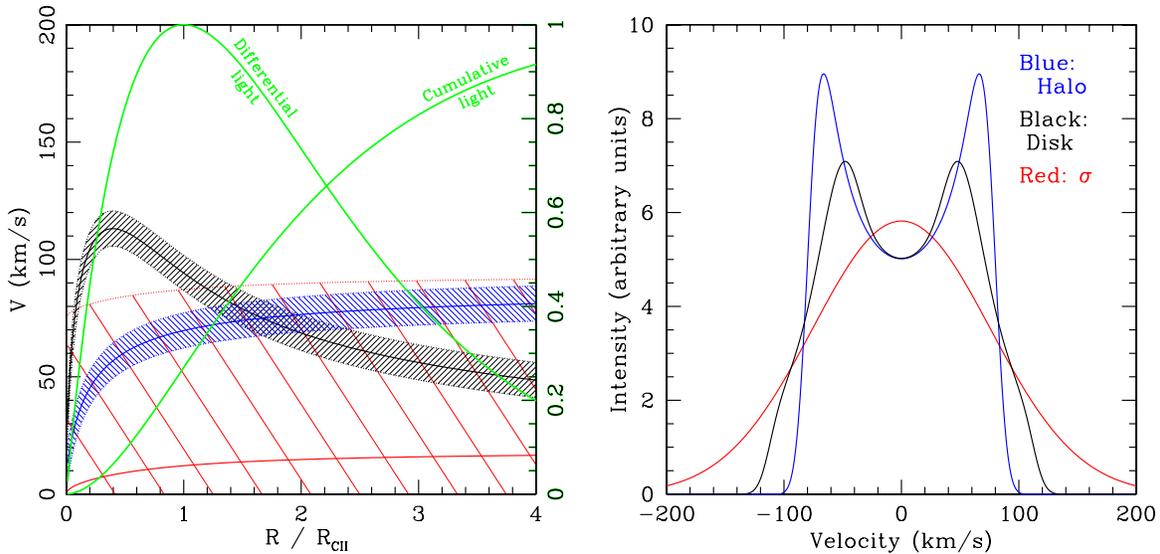
5

Figure 4. Correspondence between rotation curve and line profile for three "toy models," each of which is dominated by a single kinematic component. In both panels, blue corresponds to a halo-dominated rotation curve (with gas velocity dispersion $\sigma_g = 7.5 \, \mathrm{km \, s^{-1}}$), black to a disk-dominated rotation curve ($\sigma_g = 7.5 \, \mathrm{km \, s^{-1}}$), and red to a dispersion-dominated galaxy ($\sigma_g = 75 \, \mathrm{km \, s^{-1}}$). Left: the rotation curves (with shading for the region $v_c(r) \pm \sigma_g$). The two green curves show $dL_{[\mathrm{C\,II}]}/dr$ and its integral, $L_{[\mathrm{C\,II}]}(r)$ (i.e., the enclosed [C II] luminosity), both normalized to their respective peaks. They show how the different portions of the rotation curve are weighted in the line profile. Right: the resulting line profiles.

(A color version of this figure is available in the online journal.)

± 0.17. The 1.3% of simulations with more extreme ratios are all velocity-dispersion dominated models, where the asymmetry introduced in the magnification is hidden by the random motions of the gas. The only correlation between μ_a and other model parameters is a trivial correlation with model redshift: an offset in redshift that would move the modeled flux centroid away from the observed flux centroid can be compensated by raising the peak of the line profile that falls nearest the observed flux centroid, and lowering the amplitude of the other peak. The addition of μ_a does not alter the distributions of other model parameters in any qualitatively important way.

For the Clone, the μ_a parameter is not strongly constrained. Models having $\sigma_g < v_{c,1/2}$ generally have $0.4 < \mu_a < 2.5$, but dispersion-dominated models can yield acceptable fits with any value of μ_a. With the addition of μ_a, about 3/4 of the fits end up with $\sigma_g > v_{c,1/2}$.

We also explored the possibility of a ring-like gas distribution. We take the limiting case by assuming *all* the emitting gas rotates with a single circular speed v_c. The intrinsic line profile is then proportional to $1/\sqrt{1 - (v/v_c)^2}$, potentially modified by the differential amplification parameter μ_a described above, and convolved with a Gaussian of width σ_g to account for velocity dispersion within the ring. In total, this is a five-parameter model: $\{v_c, \sigma_g, z, f_{[\mathrm{C\,II}]}, \mu_a\}$. Qualitatively, our key results are unchanged under this model: we again find that S0901 is rotationally supported, and that the Clone admits a range of acceptable models. In closer detail, we do see some differences. The full disk models described above can smooth the line profile of a single ring both through velocity dispersion and through the combination of multiple rings with different circular speeds. The single-ring model can only soften the sharp edges of the double-horned profile through the effects of velocity dispersion. Thus, values of $\sigma_g \lesssim 30 \, \mathrm{km \, s^{-1}}$ are common in the full disk model for S0901 but rare among the single-ring fits. Similarly, the distribution of $y_{\sigma c} = \sigma_g/v_c$ tends to slightly higher values under the single-ring model. Our exploration of ringlike gas distributions leads to two main conclusions. First, the

Atacama Large Millimeter Array (ALMA) observations will be tremendously valuable in determining the spatial distribution of the emitting gas in cases like these. Second, our conclusion that S0901 is rotationally supported is robust to plausible variations in the gas geometry.

4. COMPARISON WITH Hα KINEMATICS

Both S0901 and the Clone have previously published kinematic constraints in the form of Hα line widths ($\Delta v_{\mathrm{H\alpha,obs}}$). To compare our [C II] results to these, we use our kinematic models to predict the Hα line width $\Delta v_{\mathrm{H\alpha,pred}}$ that would be expected, after accounting for the lower spectral resolutions of the published Hα observations. We do this by convolving our model line profile(s) with a Gaussian whose width $\delta\lambda_{\mathrm{LSF}}$ matches the reported line spread function (LSF) of the Hα observations, measuring the FWHM $\Delta\lambda_{\mathrm{H\alpha,conv}}$ of the convolved line profile, and calculating the LSF-corrected line width $\Delta\lambda_{\mathrm{H\alpha,pred}} = (\Delta\lambda_{\mathrm{H\alpha,conv}}^2 - \delta\lambda_{\mathrm{LSF}}^2)^{0.5}$. We finally convert the result back to velocity units for ease of comparison ($\Delta v_{\mathrm{H\alpha,pred}} = \Delta\lambda_{\mathrm{H\alpha,pred}} \times c/\lambda_{\mathrm{H\alpha}}$).

For S0901, Hainline et al. (2009) report $\Delta v_{\mathrm{H\alpha,obs}} = 308 \pm 12 \, \mathrm{km \, s^{-1}}$ (FWHM), with a spectral resolution $\delta\lambda_{\mathrm{LSF}} = 15 \, \text{Å}$ FWHM, corresponding to $210 \, \mathrm{km \, s^{-1}}$ FWHM at $2.137 \, \mu\mathrm{m}$ wavelength. For our best-fitting model, the procedure described above yields $\Delta v_{\mathrm{H\alpha,pred}} = 266 \, \mathrm{km \, s^{-1}}$. If we apply the same procedure to the full set of models produced by the MCMC fitting, the mean and standard deviation of the result becomes $\Delta v_{\mathrm{H\alpha,pred}} = 255 \pm 19 \, \mathrm{km \, s^{-1}}$. Combining in quadrature the scatter in our simulations and the uncertainty reported by Hainline et al. (2009), our models predict a line width that is smaller than the observed Hα line width at the 2σ level.

If the difference is real, there are a few possible explanations. First, the true LSF of the Keck spectrum could be 18–21 Å (250–300 km s^{-1}) FWHM, rather than the published measurement of 15 Å (210 km s^{-1}) FWHM (Hainline et al. 2009). Second, the [C II] and Hα observations might sample different portions of the galactic disk. The *Herschel* observations

certainly sample the entire galaxy, while NIRSPEC's 0″.76 slit could omit outer regions of the galactic disk. Third, the kinematics of [C II] and Hα could be genuinely different. If large velocity dispersions are associated with turbulence driven by star formation activity (Green et al. 2010; Lehnert et al. 2013), the kinematic effects of star formation would be most strongly apparent in Hα, which is closely associated with star formation activity. The PDR gas that contributes strongly to [C II] emission is found at the "skin" layers of molecular clouds and may yet retain the comparatively quiescent kinematics of molecular gas.

Hα kinematic constraints for the Clone have been reported both by Hainline et al. (2009; slit spectroscopy) and Jones et al. (2010, 2013; integral field unit (IFU) spectroscopy). To compare to Hainline et al. (2009), we followed the same procedure we used for S0901. The best-fitting model gives an expected line width of $\Delta v_{\mathrm{H}\alpha,\mathrm{pred}} = 160\,\mathrm{km\,s^{-1}}$ FWHM, while the mean and standard deviation for all the MCMC runs was $\Delta v_{\mathrm{H}\alpha,\mathrm{pred}} = 194 \pm 52\,\mathrm{km\,s^{-1}}$. The observed Hα line width is consistent with these expectations, at $\Delta v_{\mathrm{H}\alpha,\mathrm{obs}} = 188 \pm 9\,\mathrm{km\,s^{-1}}$ FWHM (again with $\delta\lambda_{\mathrm{LSF}} = 15\,\text{Å}$ FWHM).

The Hα IFU spectra reported by Jones et al. (2010, 2013) offer a more detailed comparison, with spatially resolved spectra at a spectral resolution of $52\,\mathrm{km\,s^{-1}}$. Their full measured rotation curve (i.e., the range of centroid velocities of Hα emission across the resolved image) spans $\Delta v = 159 \pm 38\,\mathrm{km\,s^{-1}}$, with a line-of-sight velocity dispersion of $104 \pm 37\,\mathrm{km\,s^{-1}}$ (Jones et al. 2013, Table 4). The results depend, again, on subtracting the instrumental LSF width in quadrature, but this time the LSF is narrower than the measured line width. The $104\,\mathrm{km\,s^{-1}}$ velocity dispersion corresponds directly to our σ_g parameter. The correspondence between the Jones et al. (2013) parameter $\Delta v = 159 \pm 38\,\mathrm{km\,s^{-1}}$ and our rotation speed parameter $v_{1/2}$ is less direct. While we roughly expect $\Delta v \approx 2v_{1/2}$, our parameter refers to the rotation speed at the half-light radius of the [C II] emission, while ΔV is measured across the full extent of the Hα emission. Still, we expect the kinematic parameters from Jones et al. (2013) to fall in the range $60\,\mathrm{km\,s^{-1}} \lesssim v_{1/2} \lesssim 80\,\mathrm{km\,s^{-1}}$ and $\sigma_g \approx 104\,\mathrm{km\,s^{-1}}$. While this is far from our *best-fitting* model for the [C II] rotation curve, it is within the 90% confidence region derived from the MCMC fitting results. The MCMC approach thus provides a better consistency check than a simple comparison of best-fit models.

5. CONCLUSIONS

Our [C II] spectra of S0901 and the Clone showcase the potential of heterodyne spectroscopy for kinematic studies of high-redshift galaxies. Förster Schreiber et al. (2009) find that about 1/3 of $z \sim 2$ galaxies are reasonably described as rotation-dominated disks, based on Hα IFU spectra. However, they are not able to resolve spectral features narrower than $\sim 60\,\mathrm{km\,s^{-1}}$. Thus, our measured upper limits on the velocity dispersion of S0901, $\sigma_g < 23\,\mathrm{km\,s^{-1}}$ ($46\,\mathrm{km\,s^{-1}}$) at 1σ (2σ), are one of the tightest limits to date on the velocity dispersion of a high-redshift galaxy. While our results are less definitive for the Clone, the maximum likelihood fits have $\sigma < 4\,\mathrm{km\,s^{-1}}$ ($14\,\mathrm{km\,s^{-1}}$) at 1σ (2σ), and 65% of our simulations yield $\Delta v/(2\sigma_g) \approx v_{1/2}/\sigma_g > 0.4$—a (semi-empirical) criterion advocated by Förster Schreiber et al. (2009) for a disk to be considered rotationally supported.

Spatially resolved observations at similar spectral resolution and S/N will be possible for some $z \gtrsim 2$ galaxies us-

ing (sub)millimeter interferometric line observations. This will enable cleaner measurements of the line-of-sight velocity dispersion. ALMA will be the most powerful such instrument for the foreseeable future, offering spectral resolution comparable to HIFI, coupled with higher sensitivity and spatial resolution as fine as $\sim 0″.2$. For our two particular objects, ALMA will not supersede our *Herschel* [C II] observations: The [C II] line in S0901 lies in a gap between ALMA's frequency bands, and the Clone is too far north ($\delta = +51°$) for ALMA observation. Fortunately, other strong lens systems will unlock the full potential of ALMA for this science.

In conclusion, the *Herschel* observations of the [C II] $158\,\mu\mathrm{m}$ line that we present here underscore the promise of the bright [C II] line as a kinematic tracer for high-redshift galaxies. They provide a unique look at the internal dynamics of two $z \approx 2$ galaxies, and show that very small internal velocity dispersions can be found in the high-redshift universe.

REFERENCES

Bennett, C. L., Fixsen, D. J., Hinshaw, G., et al. 1994, ApJ, 434, 587
Carilli, C. L., & Walter, F. 2013, ARA&A, 51, 105
Chabrier, G. 2003, PASP, 115, 763
Contursi, A., Kaufman, M. J., Helou, G., et al. 2002, AJ, 124, 751
Contursi, A., Poglitsch, A., Grácia Carpio, J., et al. 2013, A&A, 549, A118
de Graauw, T., Helmich, F. P., Phillips, T. G., et al. 2010, A&A, 518, L6
Diehl, H. T., Allam, S. S., Annis, J., et al. 2009, ApJ, 707, 686
Fadely, R., Allam, S. S., Baker, A. J., et al. 2010, ApJ, 723, 729
Förster Schreiber, N. M., Genzel, R., Bouché, N., et al. 2009, ApJ, 706, 1364
Frye, B. L., Broadhurst, T., & Benítez, N. 2002, ApJ, 568, 558
Frye, B. L., Hurley, M., Bowen, D. V., et al. 2012, ApJ, 754, 17
Green, A. W., Glazebrook, K., McGregor, P. J., et al. 2010, Natur, 467, 684
Hainline, K. N., Shapley, A. E., Kornei, K. A., et al. 2009, ApJ, 701, 52
Heiles, C. 1994, ApJ, 436, 720
Jones, T., Ellis, R., Jullo, E., & Richard, J. 2010, ApJL, 725, L176
Jones, T., Ellis, R. S., Richard, J., & Jullo, E. 2013, ApJ, 765, 48
Kramer, C., Abreu-Vicente, J., García-Burillo, S., et al. 2013, A&A, 553, A114
Law, D. R., Steidel, C. C., Erb, D. K., et al. 2009, ApJ, 697, 2057
Lehnert, M. D., Le Tiran, L., Nesvadba, N. P. H., et al. 2013, A&A, 555, A72
Lin, H., Buckley-Geer, E., Allam, S. S., et al. 2009, ApJ, 699, 1242
Madden, S. C., Geis, N., Genzel, R., et al. 1993, ApJ, 407, 579
Malhotra, S., Helou, G., Stacey, G., et al. 1997, ApJL, 491, L27
Malhotra, S., Kaufman, M. J., Hollenbach, D., et al. 2001, ApJ, 561, 766
Malhotra, S., Rhoads, J. E., Pirzkal, N., et al. 2014, ApJ, in press
McLinden, E. M., Finkelstein, S. L., Rhoads, J. E., et al. 2011, ApJ, 730, 136
Pettini, M., Shapley, A. E., Steidel, C. C., et al. 2001, ApJ, 554, 981
Pilbratt, G. L., Riedinger, J. R., Passvogel, T., et al. 2010, A&A, 518, L1
Pineda, J. L., Langer, W. D., Velusamy, T., & Goldsmith, P. F. 2013, A&A, 554, A103
Rhoads, J. E., Malhotra, S., Finkelstein, S. L., et al. 2014, ApJ, 780, 20
Shapley, A. E., Steidel, C. C., Pettini, M., & Adelberger, K. L. 2003, ApJ, 588, 65
Springob, C. M., Haynes, M. P., Giovanelli, R., & Kent, B. R. 2005, ApJS, 160, 149
Wiklind, T., Combes, F., Henkel, C., & Wyrowski, F. 1997, A&A, 323, 727
Wuyts, E., Rigby, J. R., Gladders, M. D., et al. 2012, ApJ, 745, 86